

pubs.acs.org/JACS Article

Diradicals as Topological Charge Carriers in Metal—Organic Toy Model Pt₃(HIB)₂

Maarten G. Goesten* and Leslie M. Schoop



Cite This: J. Am. Chem. Soc. 2024, 146, 29599-29608



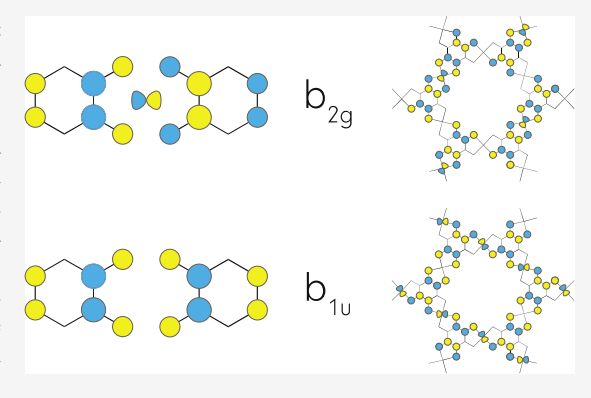
ACCESS

III Metrics & More

Article Recommendations

Supporting Information

ABSTRACT: We explore the eclipsed stacking of a metal—organic Kagome lattice containing heavy-metal nodes. Our model is $Pt_3(HIB)_2$, a hypothetical but viable member of a well-known family of hexaaminobenzene based metal—organic frameworks (MOFs). Applying space group theory, it is shown how molecular diradicals, brought into play by a noninnocent ligand, become topologically nontrivial bands when moving in a periodic potential. Three factors are required to enable this: (1) eclipsed stacking, which shifts the Fermi level near a symmetry-protected band crossing (2) the emergence of an electride-like band that renders the topological \mathbb{Z}_2 invariant equal to 1, thus nontrivial, and (3) Pt-induced spin—orbit coupling, to turn the crossing into a bulk band gap. The electride band, with its unforeseen role, bears kinship to the interlayer band in hexagonal superconductors. It places its charge density in the voids of the



crystal, rather than around the atomic nuclei, and we name it a "pore band". While the synthesis of truly conductive MOFs has proven challenging, the analysis shows that intrinsically nonlocal physics may emerge from tunable molecular building blocks. With the richness of redox-active MOF chemistry, this offers a pathway to tailored topological electronics.

■ INTRODUCTION

In topological materials, special edge or surface states give rise to lossless channels with countercurrent flow of electrons with opposite spins. This form of entanglement arises from the symmetry properties of occupied bands in reciprocal space, and the resulting topology of their mapping on Hilbert space. A nontrivial topology is associated with an odd number of band inversions in the first Brillouin Zone. Such inversions are related to reversals in energy ordering between bonding and antibonding orbitals, much like inverted ligand fields in molecules.^{1,2} In such, a band inversion may be considered a crossing between bonding and antibonding bands near the Fermi level $E_{\rm E}$, in which the latter becomes occupied. The crossings themselves are enforced by the symmetry of the lattice, and their role in topological materials demonstrates how space groups can give rise to quantum phenomena which are impossible to attain with molecules. From a chemical viewpoint, the bulk-boundary correspondence may be the strangest; it prescribes the observed appearance of metallic states at the interface of a topological insulator, and trivial insulator air, which persists in the face of lattice impurities and defects (if not too major).

These novel electronics have become well reproducible, and are being explored for application in quantum computing, spintronics, thermoelectrics, sensing, high-performance transistors, and by virtue of the quantum Hall effect, even as the new standard for the base unit of electric resistance ohm

 (Ω) .¹¹ A spectacular hypothesis argues that high-mobility topological surface states (TSS) bring high rates in heterogeneous catalysis. This defies the classical approach to transport phenomena in chemical engineering, as well as the conventional picture of a catalyst's surface, given the robustness of these states against surface modification.^{12–15} Although it is estimated that a large majority of all known materials contains topological bands,^{16,17} only a fraction provides robust and "pristine" states that are not convoluted with bulk ones. In principle, such states can be engineered through a combination of strong SOC, an appropriate lattice symmetry and delocalized chemical bonding. ^{18,19}

Metal—organic frameworks (MOFs) can give concurrent control over these properties through the careful selection of molecular building blocks. ^{20,21} Unfortunately, polar metal—ligand bonding invokes large gaps for most MOFs, and the associated electronic localization leaves no chance for highly mobile states. The search for gapless MOFs has to great extent been steered by the Dincâ group, and the conductive MOFs that have been developed are best described as semimetals,

Received: July 22, 2024
Revised: September 30, 2024
Accepted: October 1, 2024
Published: October 17, 2024





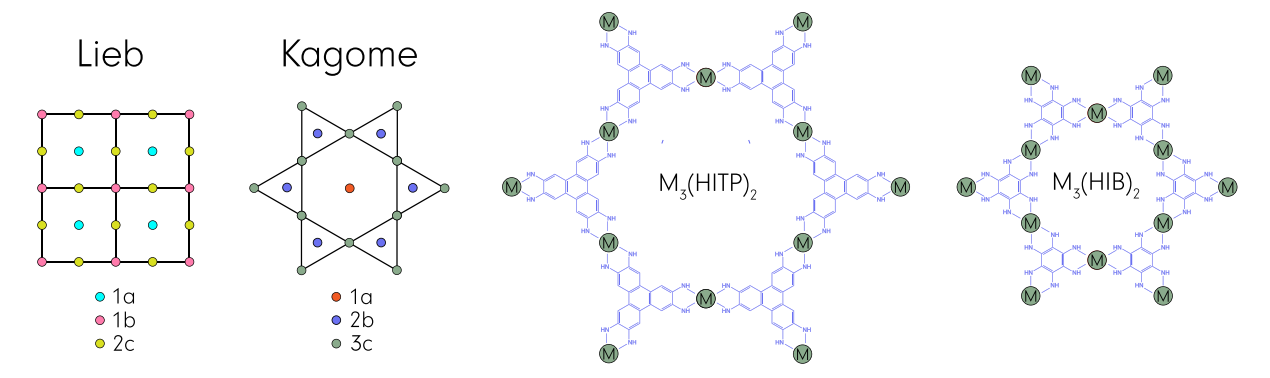


Figure 1. Left: schematic depiction of Lieb and Kagome lattices with indication of Wyckoff positions. Right: two examples of metallic Kagome MOFs, with HITP or HIB linkers in the 2b positions.

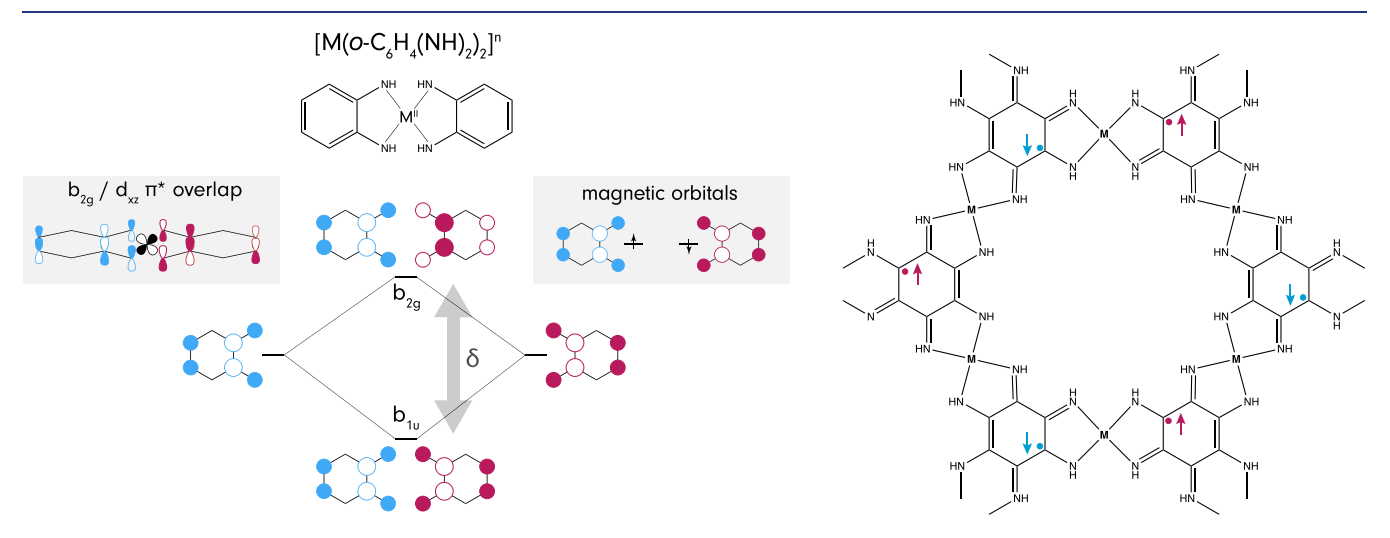


Figure 2. Left: MO diagram depicting the b_{1u} and b_{2g} orbitals of the M(HIB)₂ complex as interaction between two o-phenylenediamine fragments—the perspective depicts $2p_z$ orbitals from above (i.e., they are not 2s). The b_{2g} orbital has the appropriate symmetry for π overlap with a (Wyckoff 3c) metal ion d_{xz} orbital, and the associated antibonding interaction is what mainly controls gap δ . For the case of a neutral complex and a small gap δ , two electrons occupy the two orbitals, setting the scene for diradical character. The latter is associated with magnetic orbitals, in which opposite spins sit on different ligands. The extended framework is then expected to form a hexagonal spin—lattice, as shown by the Lewis structure on the right.

given the typically small density-of-states (DOS) at $E_{\rm F}$ ($N_{\rm EF}$). This is in fact beneficial; a large contribution to $N_{\rm EF}$ by trivial bulk states "contaminates" the detectability and control over TSS. ^{16,17}

Two types of 2D MOF nets have been probed for topological properties: the square Lieb lattice (wallpaper group: p4mm, point group: D_{4h}), and the hexagonal Kagome lattice (p6mm, point group: D_{6h}). Figure 1 depicts both lattices, as well as Wyckoff positions that indicate site-symmetry. The Wyckoff positions and local orbital symmetry control the topology of the electronic band structure.²² Each Wyckoff position is associated with a set of operations g in the crystallographic point group P that transform the position into itself, or an equivalent point. With r the position vector in real space, this is the *stabilizer* subgroup $\operatorname{Stab}_{P}(\mathbf{r})$: $\{g \in P \mid g \cdot \mathbf{r} = \mathbf{r}\}$. For example, in the two-dimensional Lieb lattice on the left in Figure 1, positions 1a and 1b are unchanged by a C_4 rotation, but 2c is not. The particularly attractive feature of MOFs is that we can often choose from multiple, chemically distinct options for every Wyckoff position, so that one could, in principle, tailor a certain band structure. In such, a MOF Lieb lattice can be synthesized with different square-planar transition metal ions at the 2c position, connecting phthalocyanine ligands at 1b.^{23–25} These lattices are predicted to become topological semimetals for specific chemical compositions, or under the application of physical strain.²⁶

Analogously, semimetallic MOF Kagome lattices can be realized with a variety of square planar transition metal ions and redox-active ligands like 2,3,6,7,10,11-hexaaminotriphenylene and hexaaminobenzene. In this hexagonal lattice, the metal ions occupy the 3c Wyckoff position, and the linkers the 2b positions—one can see this in Figure 1. Upon coordination to the metal, the ligands lose protons and "amino" turns into "imino"; the associated MOFs are usually abbreviated as $M_3(HITP)_2$ and $M_3(HIB)_2$, with HITP = hexaiminotriphenylene and HIB = hexaiminobenzene. These two frameworks are isoreticular, and can be synthesized with variations of the linker where the coordinating NH moiety is replaced by O or S. $^{30-33}$ These conductive Kagome MOFs offer a rich playground for topological electronics. $^{34-40}$

However, where graphene can be famously peeled off graphite with adhesive tape, similar solidity should not be expected for porous 2D MOFs. The synthesis of free-standing 2D MOF nets typically requires surface support, ⁴¹ the electric field effects of which may be expected to shift the position of the gap away from $E_{\rm F}$, or in fact quash observable topological

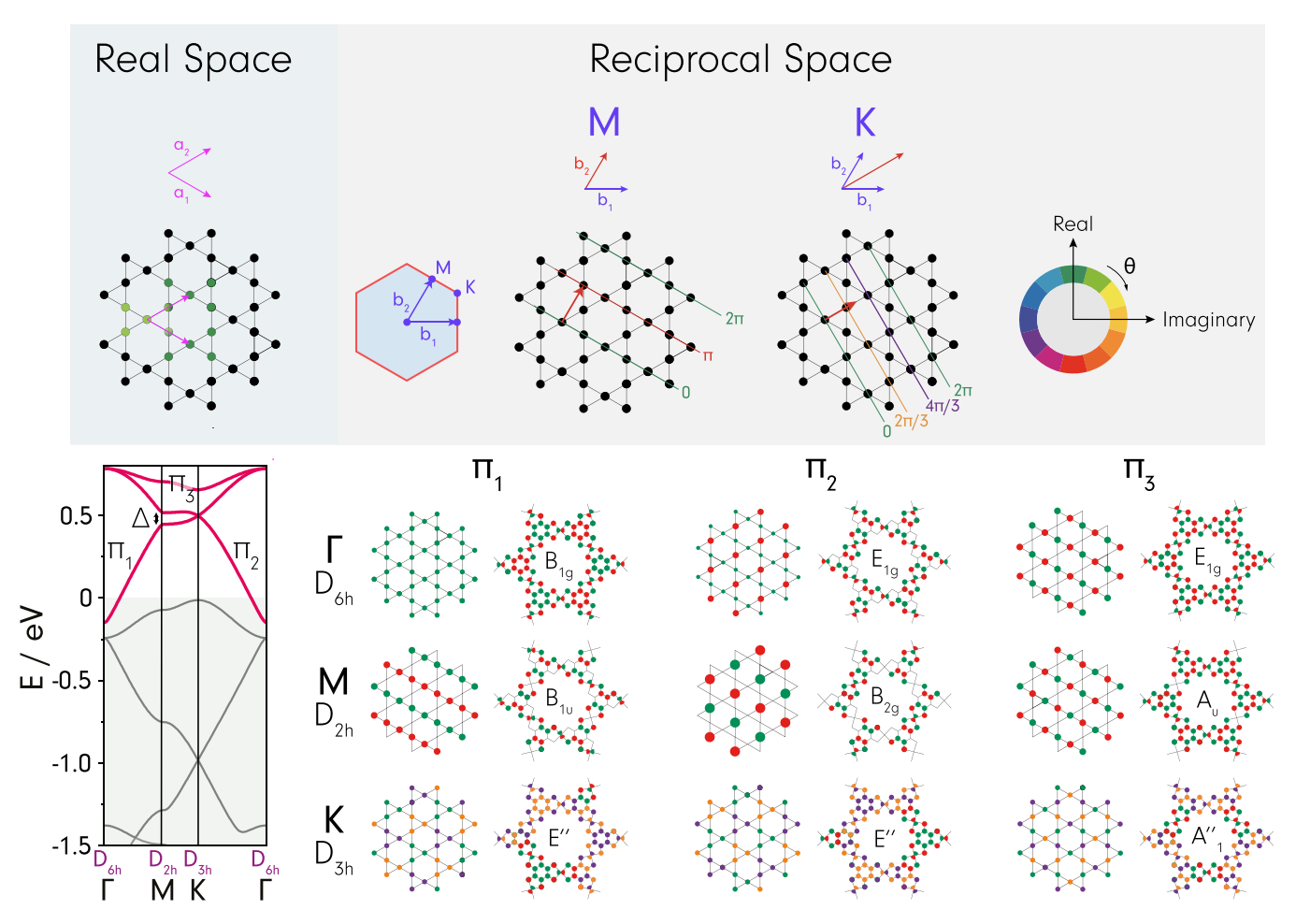


Figure 3. Top: depiction of the lattice in real space, where the lattice vectors indicate the translation of one unit cell center to the next. The unit cell can be conceived as a horizontal hourglass, with one unique lattice point, and four points shared with adjacent cells. To the right: 2D hexagonal Brillouin Zone and reciprocal-lattice vectors b_1 and b_2 defining planes of Kagome lattice points in real space. The complex phase factor associated with these planes is indicated by the angle in the color wheel to the right. Bottom left: band structure of 2D Pt₃(HIB)₂ with the three Kagome bands near E_F – π_1 , π_2 and π_3 –in red. Bottom right: representation of Kagome crystal orbitals of a simple three-point lattice basis, and to the right, the analogous orbitals of π_1 , π_2 and π_3 , which start from a π^* basis (as can be seen at Γ).

states. All Only a couple of theoretical studies focus on the stacked versions of above-described lattices, and they show that stacking can actually stabilize topological phases, by altering the energy position of $E_{\rm F}$ favorably with respect to the band structure. All 4.5,444

In this paper, we show that $Pt_3(HIB)_2$, in eclipsed stacking, is a tMOF with "strong" topological states. We will explain what "strong" means in the context of a band structure analysis. But to show how the topology of the band structure is controlled by refined metal—ligand chemistry, we start from the molecular level.

■ RESULTS AND DISCUSSION

Hexaaminobenzene Ligand and the M(HIB)₂ Complex. Hexaaminobenzene should be a redox-active linker (or *noninnocent*), from what is known for the square-planar coordination of certain + II metal ions to two *ortho*-phenylenediamine ligands. The associated complex $[M(o-C_6H_4(NH)_2)_2]^n$, with M the metal ion and n the charge, is shown on the left-hand side of Figure 2. The charge sets the number of electrons that occupy two redox-active molecular orbitals (MOs), with b_{1u} and b_{2g} irreducible representations (irreps) of the molecule's D_{2h} point group: zero electrons for n

= 2+, two for n = 0 and four for n = 2-. The b_{1u} and b_{2g} MOs are respectively the in- and out-of-phase combinations of two totally symmetric (a₁) π^* orbitals of a single C_{2v} DAB molecule (Figure 2, left, the linear combinations of 2p, orbitals are drawn from a z-axis perspective, i.e., they look like 2s combinations). The b_{2g} MO is π -antibonding with the transition metal d_{xz} orbital (occupying the Wyckoff 3c position in the extended lattice in Figure 1). This repulsive interaction is what sets the gap δ , estimated to be about 1 eV at the DFT-BP86 level for M = Ni. This special pair of orbitals is found in a family of complexes, including dithiolato [M(o- $(C_6H_4S_2)_2^n$, dicatecholato $[M(o-C_6H_4O_2)_2]^n$ and multiplering variants, where they have been employed in ligand-centered catalysis. 47-50 The HITP ligand is catalytic when embedded in the extended lattice Ni₃(HITP)₂ also,⁵¹ which shows that the electronic redox properties can be heterogenized. Ni₃(HIB)₂ and Cu₃(HIB)₂ were subsequently shown to possess stellar capacitance and durability.⁵²

The neutral complex $M(o-C_6H_4(NH)_2)_2$ with its two electrons and small gap δ , is a singlet diradical. ⁵³ Diradicals are an archetypal case of static electron correlation, and involve the coupled, *entangled* motion of two electrons with opposite spin. It is important to consider that sophisticated electronic

structure analyses have shown ligand diradicals in these complexes to interact through the Ni, via superexchange, mediated by the metal-ligand π -antibonding interaction (and gap δ). 46 DFT, a single-particle method, breaks the symmetry of the wave function to produce a density representable of the many-body system. 54,55 This leads to so-called magnetic orbitals (Figure 2, top right), which look like the interacting fragment MO's on the left of Figure 2, with spatial detachment between opposite spins. The degree of diradical character, inversely proportional to the singlet-triplet gap, controls the extent to which the opposite spins are separated, i.e., it is also inversely proportional to the overlap of the magnetic orbitals in Figure 2. Symmetry-broken DFT solutions are mathematically improper, because they do not transform as irreps of the local point group.⁵⁶ But DFT is known to produce reasonably accurate singlet-triplet gaps due to a fortunate cancellation of errors, 57 closer to experiment than (post-Hartree-Fock) CASSCF calculations involving excitations of just the two π^* electrons.⁴⁵

The diradical character can be well visualized through a Lewis structure of the extended M₃(HIB)₂ framework. This reveals a hexagonal spin-lattice, with spins in antiparallel alignment between neighboring rings (Figure 2, right). We now aim to introduce significant spin-orbit coupling (SOC) through a heavy metal ion in the Wyckoff 3c position, to lock the momentum of the charge carriers onto their spins. Multilayer $M_3(HIB)_2$ has been synthesized for M = Ni, Cu,⁵² and Co,⁵⁸ and since the related molecular [M(o- $C_6H_4(NH)_2)_2$ ⁿ complexes can be made with M = Pd, Pt as well, 3D Pt₃(HIB)₂ appears a feasible target for synthesis. Pt can be expected to invoke strong SOC, but that is not what eventually determines whether TSS appear. For that, we need this MOF to (1) provide a linearly dispersed and gapped Dirac crossing at or near E_F and (2) offer a topologically nontrivial band structure.

Single-Layer Pt₃(HIB)₂ and Time-Reversal Symmetry. The structural relaxation of single-sheet Pt₃(HIB)₂ with DFT-PBE gives Pt–N bond lengths of 2.00 Å, in line with those observed in the molecular analogues described above. The Computational Methods section, at the end of the paper, details all calculations. The (next nearest-neighbor) N–N distances are 2.52 and 3.10 Å, between N's on the same and different ligands, respectively.

The band structure of 2D $Pt_3(HIB)_2$ shows, near E_F , a pattern characteristic for the Kagome net.⁶⁰ It is shaped by three π bands $-\pi_1$, π_2 and π_3 —that are shown in the bottom left of Figure 3 in pink. We start by analyzing this motif, and apply Bloch's Theorem, as well as Zak's approach of defining the band structure as a set of localized orbitals that are invariant under all operations of the space group. Thus, our one-electron Bloch functions take the form $\psi_k(r) = e^{i\mathbf{k}\cdot\mathbf{r}}u(\mathbf{r})$, where \mathbf{r} is the position vector in a periodic basis function $u(\mathbf{r})$, a linear combination of atomic orbitals (LCAO) for which holds $u(\mathbf{r} +$ \mathbf{R}) = $u(\mathbf{r})$, with \mathbf{R} a lattice vector. We will refer to the LCAO description of $\psi_k(\mathbf{r})$ as a *crystal orbital*. The wave vector \mathbf{k} sets the phase factor $e^{i\mathbf{k}\cdot\mathbf{r}}$, and with that the local point group of which $\psi_k(\mathbf{r})$ forms a representation. This is the stabilizer subgroup in reciprocal space, the set of operations that transforms k into itself: $\operatorname{Stab}_{P}(\mathbf{k})$: $\{g \in P \mid g \cdot \mathbf{k} = \mathbf{k}\}$. We call it the group of k. In the center of the Brillouin Zone, by definition, this group is equivalent to the full crystallographic point group of the lattice: D_{6h} . At all other points in the Brillouin Zone, it will be a subgroup of D_{6h} (including D_{6h} itself).

Note that at most points in the Brillouin Zone, **k** will only be transformed into itself by the identity operation E; the group of **k** is then trivial, and $\psi_k(\mathbf{r})$ forms a representation of the C_1 point group. But at high-symmetry points, the group of **k** will be larger.

Figure 3 shows how this works. At high-symmetry point M, k defines planes of lattice points that correspond to fully real phase factors $e^{in\pi}$ (n an integer, i.e., $n \in \mathbb{Z}$); the 6-fold rotation becomes 2-fold, and k has the D_{2h} point group. At K however, this is the D_{3h} point group, with no inversion, and the $e^{2in\pi/3}$ factors and therefore $\psi_k(\mathbf{r})$ are necessarily complex. This is an important property of the hexagonal lattice, and the presence or absence of the inversion center will be of significance our upcoming analysis of the topological invariant. For now, we see that a correct real-space representation of the crystal orbital in Hilbert space requires depiction of the complex phase angle, and we do this in Figure 3 through Itten's color wheel.

A simple, general representation of Kagome crystal orbitals, as shown in Figure 3, employs a three-point (Wyckoff 2c, Figure 1) lattice basis, following what Johnston and Hoffmann obtained for the Kagome boron net. 61 Our system is a bit more complex, and multiple LCAOs can serve as basis $u(\mathbf{r})$ for three Kagome bands to develop; the pattern will be the same. But we know that the Kagome crystal orbitals near E_F should resemble the frontier MOs of Figure 2. Thus, we pick $u(\mathbf{r})$ to have πp_z p_z C-C, π^* p_z/p_z N-C, and π^* p_z/d_{xz} N-Pt interactions. The corresponding crystal orbitals (that belong to the red Kagome bands) are shown to the right of the general representations, and they are denoted by the irreps of the local point group. The π_1 crystal orbital, with delocalized $\pi p_z/p_z$ C–C across the rings, takes up the B_{1g} irrep. The π_2 & π_3 degenerate E_{1g} crystal orbitals then follow from the introduction of a nodal plane that dissects the aromatic rings at Wyckoff 2b positions. These planes are orthogonal (with respect to each other).

Between Γ and M, the π_1 band gains significant energy, the π_2 moves down in energy to a lesser degree, and the π_3 stays practically flat, as it does throughout the Brillouin Zone. Knowing $u(\mathbf{r})$ allows us to identify the interactions that control the dispersion. The π_1 band increases in energy, because the appearance of nodal planes in all aromatic rings (at loss of C-C π -bonding interactions) wins out over the loss of one antibonding p_z/d_{xz} interaction per unit cell. The π_2 band just loses two of those antibonding interactions per unit cell, which is why it goes down in energy. At M, the π_1 and π_2 bands have become extended-structure analogues of the b_{1u} and b_{2g} MOs of Figure 2. The energy gap between the two states, Δ in Figure 3, comes off a Pt-N antibonding interaction that is present for $B_{2\sigma}$, but not for $B_{1\eta}$. Δ for the MOF is considerably smaller than δ for the molecule (Figure 2). This is due to "half antibonding" interactions (with just one N per interaction), that are enforced by the translational symmetry for B_{1u}. In addition, relativistic contraction of the Pt 5d orbitals should lower the overlap, and in such weaken the antibonding interaction that mediates the energy gap between the two orbitals, as well as the superexchange. Previously reported band structures show a smaller computed Δ for Pt as compared to Ni (in bilayer analogues based on thiolato ligands).4

Between M and K, both bands become almost perfectly flat, until they meet each other at the symmetry-protected degeneracy at K. This degenerate E" irrep at K is also found in graphene, graphite and several hexagonal superconductors. From M to K, two rings lose two nodal planes, and one ring gains three nodes of a $2\pi/3$ phase angle. The latter correspond

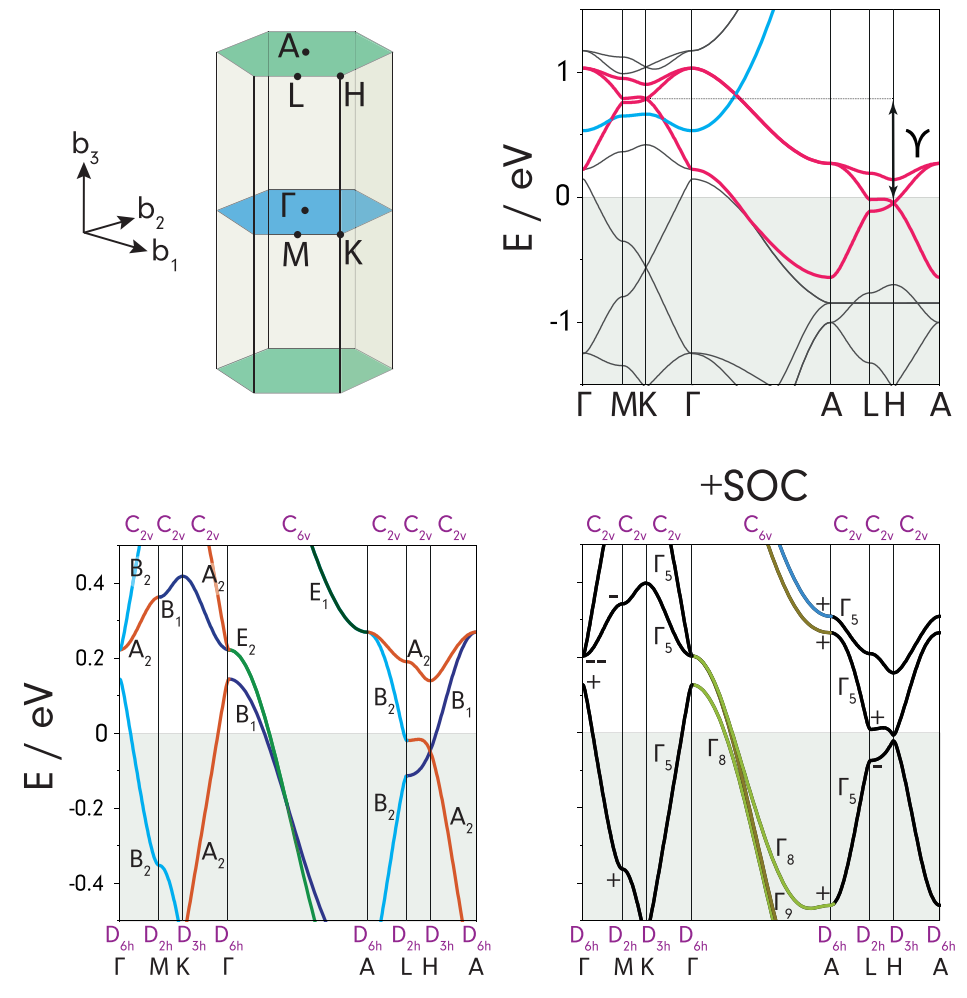


Figure 4. Top left: schematic Brillouin Zone of 3D $Pt_3(HIB)_2$ in eclipsed stacking. Top right: corresponding band structure over a wide energy range, with the Kagome bands highlighted in red. Their dispersion over b_3 , the stacking direction, corresponds to denoted energy Υ . The "pore" band is drawn in blue. Bottom: band structures without and with spin—orbit coupling (+SOC), with irreps along the band structure, and depicted through different colors.

to three antibonding interactions with half the overlap, per $S_{\Delta\theta} = S_0 \cos{(\theta)}$, where S_0 is the overlap between two orbitals with no difference in phase $(\theta = 0)$ i.e., three "half antibonding" interactions.

The flat π_3 band is sometimes referred to as a Chern band in the modern literature, $^{42,62,63}_{,}$ and "flat topological bands" are a topic of current interest. The π_3 band, along Γ -M, loses just one antibonding p_z/d_{xz} interaction per unit cell, and thus remains higher up in energy than the π_2 band, which lost two (one could say the band remains a bit flatter than this LCAO depiction would fully explain). From M to K, the rings lose the single nodal plane dissecting them, and form three pairs of p_z orbitals with the complex phase difference of $2\pi/3$ between. The ring C–C π -bonding sees *some* stabilization, as we move from two antibonding interactions per ring, to three "half antibonding" ones. But the reintroduction of π^* p_z/d_{xz} interactions gets net stabilization to be marginal overall, and leaves the band flat.

The orbital analysis shows that the framework band structure near the crossing of the π_1 and π_2 bands at K is controlled by the same antibonding interactions that mediate superexchange between diradicals in the M(HIB)₂ molecular complex. Because Δ between the π_1 and π_2 bands at M is as much as an order of magnitude smaller than δ in Figure 2, we

must have diradical character in these bands in case $E_{\rm F}$ were near the crossing. For single-layer ${\rm Pt_3(HIB)_2}$, that last condition does clearly not hold. But things change when layers are stacked in an eclipsed mode.

3D Pt₃(HIB)₂ and the Topological Invariant. London dispersion interactions are expected to be significant between layers. We treat these with Grimme's correction to PBE-DFT, and compute the eclipsed stacking enthalpy of Pt₃(HIB)₂ to amount to ~30 meV/atom, with an equilibrium interlayer distance of 3.5 Å. Electron diffraction has experimentally revealed an eclipsed (*P*₆/*mmm*) stacking for both Ni₃(HIB)₂ and Cu₃(HIB)₂ at room temperature conditions.⁵² Yet a recent study of the HITP analogues, by Berry et al., reveals stacking defects at 100 K, which the authors relate to the absence of an electronically ordered state in their measurements down to 0.1 K.⁶⁵ We return to discuss the challenge of synthesizing (near)-perfectly stacked Pt₃(HIB)₂ at the end of the paper—for now we note that we are looking at a *realistic toy model*.

Figure 4 shows the calculated band structure of 3D $Pt_3(HIB)_2$. In this hexagonal BZ, the three-band pattern of Figure 3 appears twice (Figure 4, top right), both patterns shifted by an energy Υ . The Υ term scales, quantitively, with the magnitude of interlayer orbital interactions, i.e., electronic band dispersion along the Γ -A segment in which the interlayer

 σ p_z-p_z interaction changes sign (from antibonding to bonding). For Pt₃(HIB)₂, it is a large value for Υ which puts the symmetry-protected crossing near $E_{\rm F}$, at points H in the Brillouin Zone. Note how the crossing at K has moved up in energy with respect to what is seen in Figure 3, due to interlayer antibonding interactions. This computed pattern appears regardless of the level of theory used, i.e., the same result is obtained with the hybrid HSE06 functional (Supporting Information: Section SI, Figure S1). Most importantly, $E_{\rm F}$ now lies close enough to the B_{1u} and B_{2g} orbitals and their small gap Δ : the associated bands must correspond to metallic states with diradical character.

Curiously, there is also an entirely new band that emerges upon stacking. This band is drawn in blue in the plot, cuts right through the Kagome bands and increases steeply in energy between Γ and A. This turns out to be a new type of *interlayer* band, which needs some special consideration, not least because this band will turn out to be rather important. Interlayer bands were first described in the 1980s, for graphite, graphite intercalation compounds and hexagonal boron nitride.66-68 Their role in several hexagonal superconductors, such as MgB2, CaC6 and ThSi2, subsequently initiated a revival of interest during the first decade of this century. 69,70 In an interlayer band, the charge density is not centered around atomic nuclei, but spread throughout the space between the layers and in particular, it is located at the centers of the rings at Wyckoff 1a positions in Figure 1. This is similar to what is seen in electrides, or interstitial charge localization at nonnuclear crystallographic sites. 71,72 The characteristic dispersion of an interlayer band is that of an unbound electron.⁶⁹ In our case, the unoccupied Wyckoff 1a position is actually the tubular pore, made available by eclipsed stacking. The band places charge density in the pore channels (Supporting Information, Section SII), and we therefore refer to it as the pore band. We introduce two simple methods to identify the pore band (or any interlayer band). The first applies representation theory, and uses the notion that a band corresponding to an unbound, spherically symmetric electron, must always correspond to a totally symmetric irrep of the local point group (Supporting Information, Section SIII). The second makes use of the limitations of an LCAO basis set: atom-centered basis sets without diffuse functions should have trouble to describe the pore band correctly. Indeed, where the huge QZ4P basis set gives good agreement with plane-wave calculations, the band disappears entirely at the DZP level (this is shown in Section SV of the Supporting Information). The electrons in this band still experience considerable stabilization with respect to the vacuum level—we estimate this to be almost 3 eV at Γ . And the lowest-energy pore band levels lie only half an eV above $E_{\rm F}$, making this band more accessible than the interlayer band in graphite (>2 eV).69

The bottom part of Figure 4 zooms in on the band structure near $E_{\rm F}$ at both the scalar and full relativistic level; the latter includes SOC. Regardless of the SOC's magnitude, the difference between the scalar and full relativistic level is significant from the perspective of representation theory. Only in the latter case do we consider the actual spin of the electron, an aspect often required for the topological analysis. Being a Fermion, an electron is periodic in 4π rather than 2π , meaning a 2π rotation $\mathcal R$ has a different representation than a 4π rotation, which is equivalent to the identity E. This gives rise to double point groups. Double groups tend to have more bands with the same irrep, which allows them to mix, and avoid

crossings. This can be seen in Figure 4. On all paths connecting high-symmetry points A, L and H, the group of $\bf k$ is C_{2v} . At the scalar relativistic level, the two bands that cross and set the degeneracy at H are only allowed to do so because they transform differently in that point group when approaching H (A₂ and B₁); this is the von Neumann–Wigner theorem. But when we consider spin and take the C_{2v} double point group, the two bands have the same Γ_5 irrep. The avoided crossing and associated gap are the hallmark features of a topological insulator. At 16 meV, our gap is small, because the orbitals that control it are mainly located on the organic ligands. The value is in the range of computed SOC-induced gaps for these frameworks in earlier works. SOC-induced gaps for these frameworks in earlier works. Most significantly, our calculations show E_F to be in or at least very near this gap, grazing the tip of the upper band.

For high-symmetry points where **k** is fixed by the inversion operation, double group irreps correspond to parity eigenvalues. These show up as "+" and "-", even and odd, which means as much as "gerade" and "ungerade" in the classical g and u subscript from MO notation. At D_{2h} L, B_{1u} and B_{2g} respectively become Γ_5^- and Γ_5^+ in the double group. Whenever inversion symmetry is lost, around, both levels are Γ_5 . At H, D_{3h} with no inversion, the degeneracy breaks up into Γ_7 and Γ_9 levels, setting the local gap. To determine whether the band structure is topologically nontrivial, we make use of the method by Fu and Kane for crystals with inversion symmetry. For that, we first define one set of occupied (or partially occupied) bands, as well as one set of unoccupied ones. We show these on the left-hand side of Figure 5, in respectively orange and blue. The sets are fully disentangled in the presence of SOC, because the pore band engages into an

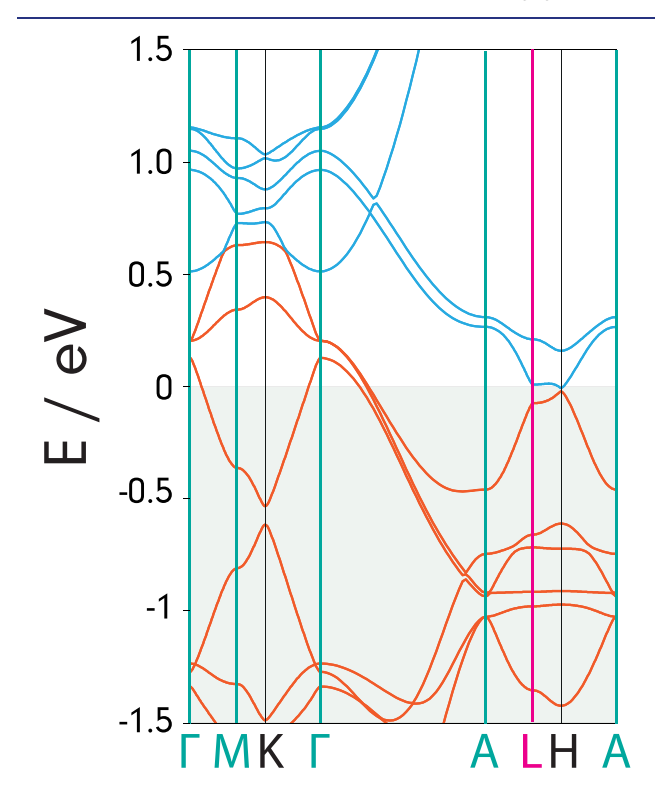


Figure 5. Band structure of 3D $Pt_3(HIB)_2$ at the full relativistic level of theory, with closed manifolds of occupied (orange) and unoccupied (blue) bands. High-symmetry points that are also time-reversal invariant have thicker, colored vertical lines. The color indicates the value for $\delta(\overline{I_i})$, turquoise if -1 and magenta if +1.

avoided crossing with the Kagome bands. For the occupied set, we now factor the parity eigenvalues at every point in the Brillouin Zone where the local point group contains an inversion operation. These high-symmetry points are referred to as time-reversal invariant momenta (TRIM): they are $1x \Gamma$, A (D_{6h}) , and 3x M and L (D_{2h}) . Note that D_{3h} K and H are no TRIM points. By virtue of Fu and Kane, the \mathbb{Z}_2 topological invariant ν follows from $(-1)^{\nu} = \prod_{BZ} \delta(\mathbb{T}_i)$, where $\delta(\mathbb{T}_i) = \pm 1$. \mathbb{Z}_2 represents "odd" and "even", and $\delta(\mathbb{T}_i)$ is effectively obtained by counting the number bands with odd parity in the occupied set, at TRIM point \mathbb{T}_i . If this number itself is odd, $\delta(\mathbb{T}_i) = -1$, and for an even number, $\delta(\mathbb{T}_i) = 1$. The product over all points \mathbb{T}_i in the Brillouin Zone then gives ν_i which indicates a "strong" topological phase when equal to unity. The descriptor distinguishes between strong topological insulators, like Sb₂Te₃, and "weak" ones, for which $\nu = 0$, like Sb₂Se₃. We find $\delta(\Gamma) = \delta(M) = \delta(A) = -1$, $\delta(L) = 1$, thus $(-1)^{\nu} = -1$ and $\nu = 1$. We underline an important role for the pore band here. Through its avoided crossing, it is part of the occupied set of bands at M, but not at Γ . As shown in the Supporting Information, Section SIV, which lists the band parity eigenvalues, this turns out to be crucial for the \mathbb{Z}_2 invariant. In conclusion, our analysis predicts strong TSS to appear in the gap at H.

Note on Experiment. The topological electronics that we describe, predict and relate to diradicals, need perfectly eclipsed stacking with P_6/mmm symmetry. The 6-fold rotational symmetry is particularly important, as it enforces the crossing at H. There is evidence for average structures to take up the eclipsed stacking at room temperature, 52 but there are also descriptions of an absence of truly metallic behavior, and relating this to stacking imperfections.⁶⁵ Topological electronics, as well as advanced techniques for the characterization of surface states like angle-resolved photoemission spectroscopy (ARPES), require large, high-quality crystals. These have long remained challenging to obtain for MOFs, but there has been serious progress in this regard. We note that the Dincă group published a modulator-based synthesis protocol for single crystals of M₃(HITP)₂ (Figure 1) and analogues.³³ They subsequently showed that conducting MOF crystals of up to 200 μ m can be grown, if one can get the ligand-metal interaction to be more reversible during crystallization, so that in-plane crystallinity is improved.⁷⁵ This elegant method aligns with James Wuest's strategy of achieving large porous crystals by optimizing the bond strength between the building blocks (tectons) that form the lattice.

An ideal, or an ideal enough stacking may well be achieved by a clever use of solvents that are employed as structure-directing molecules. Gu et al. have developed a handy and, as has turned out, widely applicable strategy to control eclipsed and rotational stacking of 2D MOF lattices with striking accuracy. While complex Moiré shapes can be engineered with proper polar solvents, apolar ones are shown to drive highly ordered eclipsed stacking. And because MOFs are highly tunable, a variety of such structure-directing strategies seems currently available. We note a very recent work in which the introduction of bulky side groups on ligands enabled a precise control of stacking and commensurate spin behavior. The associated MOFs are based on a hexaiminotriindole ligand, a yet larger analogue of HITP.

The diradical character may be probed through a transition that has been observed for molecular analogues, where it appears in the near-IR region. 46,81 It corresponds to a ligand-to-ligand charge transfer, in which adjacent linkers obtain alternating charges. For small MOF crystals, the characterization by light absorption is possible, and so is the detection of TSS by scanning tunneling microscopy.

CONCLUSIONS

We have investigated the electronic structure of $Pt_3(HIB)_2$, and shown how nonlocal framework chemistry appears upon the assembly of diradical building blocks. For this MOF, as should be the case for this entire family of MOFs, the Kagome band dispersion is controlled through (weak) π^* antibonding interactions between ligand and metal. These interactions mediate superexchange through the metal node, between diradicals localized on the organic struts. In the scenario of eclipsed stacking, the Fermi level shifts to a position where these levels belong to free framework charge carriers. We predict the Kagome band to shape a Dirac cone at H, which becomes gapped in the presence of strong SOC that is brought upon the system by Pt. An analysis of the topological \mathbb{Z}_2 invariant suggests that robust TSS must appear within that gap.

There is a special role for a pore band there, a type of interlayer band that is itself an apparent case of nonlocality. This band corresponds to a charge density that is not centered around nuclei, but rather within the tubular pores of the system, and between layers. It plays a surprisingly significant role, in rendering the system topologically nontrivial, i.e., without pore band, the \mathbb{Z}_2 invariant would be equal to zero. The pore band is energetically easier to access than the interlayer band in graphite and will become occupied upon a small degree of electron doping. This may be a way to engineer superconductivity, in particular if concepts from hexagonal intercalated superconductors can be applied. The low energy position of the pore band should make it rather interesting for (electro)catalysis as well, because we could think, at least theoretically, of a new type of heterogeneous catalysis that does not take place on metal sites or their ligands, but in the empty space of the pore. Like the interlayer band, it should be possible to detect the pore band experimentally, e.g., through X-ray absorption or scanning tunneling microscopy. 82,83 We predict the band to be there for isostructural Ni₃(HIB)₂ as well (Supporting Information, Section SV), and it is likely that some form of this band exists for a much wider range of MOFs, as well as COFs. We also note that a porous topological semimetal offers new opportunities for quantum materials in a broader sense. A MOF with a topologically nontrivial band structure, like Pt₃(HIB)₂, brings the intriguing possibility for TSS on inner pore walls, i.e., the interior surface. Filling the pore with an appropriate substrate could then constitute a new type of interface between domains.

The direct connection between diradical chemistry and topological states gives chemical control over nonlocal physics; we know states to becomes more delocalized upon increasing the diradical character, which we also know to scale along S < NH < O for organic linker substituents. Given MOFs and their building blocks offer direct control over orbitals at Wyckoff positions in real space, they offer an ideal playground for topological quantum chemistry. We therefore hope this work motivates the pursuit of synthesizing highly perfect, electronically conductive MOF crystals. Eclipsed-stacked Pt₃(HIB)₂ is a toy model, but a realistic one. Its realization

would be highly compelling for a variety of electronic applications.

COMPUTATIONAL METHODS

GGA-PBE Kohn-Sham density functional theory was used throughout. The pw.x module of Quantum Espresso 6.5 (QE) was used for variable-cell nuclear relaxation on a $6 \times 6 \times 12$ electronmomentum mesh, with tight convergence thresholds for the forces (1 × 10-4 Ry/bohr). 84,85 All calculations with QE employed Rappe-Rabe-Kaxiras-Joannopoulos ultrasoft scalar and full-relativistic pseudopotentials with a plane-wave cutoff energy of 100 Ry, with a Gaussian smearing of 0.03 Ry. 86 Grimme's third dispersion correction (D3) was applied.⁸⁷ The calculation of irreducible representations at different points of the Brillouin Zone was done with the bands.x module of QE. In AMS BAND,88 the wave functions are expanded using Slater-type orbital basis sets, varying from DZP (double- ζ with one polarization function, the smallest) and QZ4P (quadruple-ζ, with four polarization functions). The quadratic tetrahedron method was used for the k-mesh, 89 with 17 k-points along each lattice vector. Relativistic effects were accounted for by the scalar zeroth-order regular approximation to the Dirac equation (ZORA).

ASSOCIATED CONTENT

Supporting Information

The Supporting Information is available free of charge at https://pubs.acs.org/doi/10.1021/jacs.4c09993.

Full list of band irreducible representations; all-electron ZORA-HSE06/DZP band structure of $Pt_3(HIB)_2$; band parity eigenvalues; computed crystal orbital of the pore band at Γ ; band structures with STO basis referenced against the vacuum level and comparison between $Pt_3(HIB)_2$ and $Ni_3(HIB)_2$; crystal coordinates (PDF)

AUTHOR INFORMATION

Corresponding Author

Maarten G. Goesten – Department of Chemistry, Aarhus University, Aarhus 8000, Denmark; ocid.org/0000-0003-1296-0255; Email: maarten.goesten@chem.au.dk

Author

Leslie M. Schoop – Department of Chemistry, Princeton University, Princeton, New Jersey 08544, United States; occid.org/0000-0003-3459-4241

Complete contact information is available at: https://pubs.acs.org/10.1021/jacs.4c09993

Notes

The authors declare no competing financial interest.

ACKNOWLEDGMENTS

M.G.G. acknowledges Villum Fonden for funding this project through a Villum Young Investigator award, grant number 42124. L.M.S. was supported by NSF, grant OAC-2118310, the David and Lucille Packard foundation, and the Princeton Catalysis initiative.

REFERENCES

- (1) Hoffmann, R.; Alvarez, S.; Mealli, C.; Falceto, A.; Cahill, T. J.; Zeng, T.; Manca, G. From Widely Accepted Concepts in Coordination Chemistry to Inverted Ligand Fields. *Chem. Rev.* **2016**, *116* (14), 8173–8192.
- (2) Schoop, L. M.; Pielnhofer, F.; Lotsch, B. V. Chemical Principles of Topological Semimetals. *Chem. Mater.* **2018**, 30 (10), 3155–3176.

- (3) Harle, N.; Shtanko, O.; Movassagh, R. Observing and Braiding Topological Majorana Modes on Programmable Quantum Simulators. *Nat. Commun.* **2023**, *14* (1), 2286.
- (4) He, Q. L.; Hughes, T. L.; Armitage, N. P.; Tokura, Y.; Wang, K. L. Topological Spintronics and Magnetoelectronics. *Nat. Mater.* **2022**, 21 (1), 15–23.
- (5) Müchler, L.; Casper, F.; Yan, B.; Chadov, S.; Felser, C. Topological Insulators and Thermoelectric Materials: Topological Insulators and Thermoelectric Materials. *Phys. Status Solidi RRL* **2013**, 7 (1–2), 91–100.
- (6) Fu, C.; Sun, Y.; Felser, C. Topological Thermoelectrics. *APL Mater.* **2020**, 8 (4), 040913.
- (7) Zhang, M.; Wang, X.; Song, F.; Zhang, R. Layered Topological Insulators and Semimetals for Magnetoresistance Type Sensors. *Adv. Quantum Technol.* **2019**, *2*, 1800039.
- (8) Zhao, F.; Zhou, S.; Zhang, Y. Ultrasensitive Detection of Hydrogen Peroxide Using Bi ₂ Te ₃ Electrochemical Sensors. *ACS Appl. Mater. Interfaces* **2021**, 13 (3), 4761–4767.
- (9) Gilbert, M. J. Topological Electronics. Commun. Phys. 2021, 4 (1), 70.
- (10) Pirie, H.; Sadhuka, S.; Wang, J.; Andrei, R.; Hoffman, J. E. Topological Phononic Logic. *Phys. Rev. Lett.* **2022**, *128* (1), 015501.
- (11) Okazaki, Y.; Oe, T.; Kawamura, M.; Yoshimi, R.; Nakamura, S.; Takada, S.; Mogi, M.; Takahashi, K. S.; Tsukazaki, A.; Kawasaki, M.; Tokura, Y.; Kaneko, N.-H. Quantum Anomalous Hall Effect with a Permanent Magnet Defines a Quantum Resistance Standard. *Nat. Phys.* **2022**, *18* (1), 25–29.
- (12) Chen, H.; Zhu, W.; Xiao, D.; Zhang, Z. CO Oxidation Facilitated by Robust Surface States on Au-Covered Topological Insulators. *Phys. Rev. Lett.* **2011**, *107* (5), 056804.
- (13) Rajamathi, C. R.; Gupta, U.; Kumar, N.; Yang, H.; Sun, Y.; Süß, V.; Shekhar, C.; Schmidt, M.; Blumtritt, H.; Werner, P.; Yan, B.; Parkin, S.; Felser, C.; Rao, C. N. R. Weyl Semimetals as Hydrogen Evolution Catalysts. *Adv. Mater.* **2017**, *29* (19), 1606202.
- (14) Rajamathi, C. R.; Gupta, U.; Pal, K.; Kumar, N.; Yang, H.; Sun, Y.; Shekhar, C.; Yan, B.; Parkin, S.; Waghmare, U. V.; Felser, C.; Rao, C. N. R. Photochemical Water Splitting by Bismuth Chalcogenide Topological Insulators. *ChemPhysChem* **2017**, *18* (17), 2322–2327.
- (15) Li, G.; Xu, Q.; Shi, W.; Fu, C.; Jiao, L.; Kamminga, M. E.; Yu, M.; Tüysüz, H.; Kumar, N.; Süß, V.; Saha, R.; Srivastava, A. K.; Wirth, S.; Auffermann, G.; Gooth, J.; Parkin, S.; Sun, Y.; Liu, E.; Felser, C. Surface States in Bulk Single Crystal of Topological Semimetal Co ₃ Sn ₂ S ₂ toward Water Oxidation. *Sci. Adv.* **2019**, *5* (8), No. eaaw9867.
- (16) Vergniory, M. G.; Elcoro, L.; Felser, C.; Regnault, N.; Bernevig, B. A.; Wang, Z. A Complete Catalogue of High-Quality Topological Materials. *Nature* **2019**, *566* (7745), 480–485.
- (17) Vergniory, M. G.; Wieder, B. J.; Elcoro, L.; Parkin, S. S. P.; Felser, C.; Bernevig, B. A.; Regnault, N. All Topological Bands of All Nonmagnetic Stoichiometric Materials. *Science* **2022**, *376* (6595), No. eabg9094.
- (18) Hasan, M. Z.; Kane, C. L. Colloquium: Topological Insulators. *Rev. Mod. Phys.* **2010**, 82 (4), 3045–3067.
- (19) Gibson, Q. D.; Schoop, L. M.; Muechler, L.; Xie, L. S.; Hirschberger, M.; Ong, N. P.; Car, R.; Cava, R. J. Three-Dimensional Dirac Semimetals: Design Principles and Predictions of New Materials. *Phys. Rev. B* **2015**, *91* (20), 205128.
- (20) Kalmutzki, M. J.; Hanikel, N.; Yaghi, O. M. Secondary Building Units as the Turning Point in the Development of the Reticular Chemistry of MOFs. *Sci. Adv.* **2018**, *4* (10), No. eaat9180.
- (21) Chen, T.; Wang, F.; Cao, S.; Bai, Y.; Zheng, S.; Li, W.; Zhang, S.; Hu, S.; Pang, H. In Situ Synthesis of MOF-74 Family for High Areal Energy Density of Aqueous Nickel—Zinc Batteries. *Adv. Mater.* **2022**, 34 (30), 2201779.
- (22) Bradlyn, B.; Elcoro, L.; Cano, J.; Vergniory, M. G.; Wang, Z.; Felser, C.; Aroyo, M. I.; Bernevig, B. A. Topological Quantum Chemistry. *Nature* **2017**, *547* (7663), 298–305.
- (23) Abel, M.; Clair, S.; Ourdjini, O.; Mossoyan, M.; Porte, L. Single Layer of Polymeric Fe-Phthalocyanine: An Organometallic Sheet on

- Metal and Thin Insulating Film. J. Am. Chem. Soc. 2011, 133 (5), 1203-1205.
- (24) Zhou, J.; Sun, Q. Magnetism of Phthalocyanine-Based Organometallic Single Porous Sheet. J. Am. Chem. Soc. 2011, 133 (38), 15113–15119.
- (25) Zhou, J.; Wang, Q.; Sun, Q.; Kawazoe, Y.; Jena, P. Strain-Induced Spin Crossover in Phthalocyanine-Based Organometallic Sheets. *J. Phys. Chem. Lett.* **2012**, *3* (21), 3109–3114.
- (26) Jiang, W.; Zhang, S.; Wang, Z.; Liu, F.; Low, T. Topological Band Engineering of Lieb Lattice in Phthalocyanine-Based Metal—Organic Frameworks. *Nano Lett.* **2020**, *20* (3), 1959–1966.
- (27) Sheberla, D.; Sun, L.; Blood-Forsythe, M. A.; Er, S.; Wade, C. R.; Brozek, C. K.; Aspuru-Guzik, A.; Dincă, M. High Electrical Conductivity in Ni ₃ (2,3,6,7,10,11-Hexaiminotriphenylene) ₂, a Semiconducting Metal—Organic Graphene Analogue. *J. Am. Chem. Soc.* 2014, 136 (25), 8859–8862.
- (28) Campbell, M. G.; Sheberla, D.; Liu, S. F.; Swager, T. M.; Dincă, M. Cu ₃ (Hexaiminotriphenylene) ₂: An Electrically Conductive 2D Metal-Organic Framework for Chemiresistive Sensing. *Angew. Chem., Int. Ed.* **2015**, 54 (14), 4349–4352.
- (29) Dou, J.-H.; Sun, L.; Ge, Y.; Li, W.; Hendon, C. H.; Li, J.; Gul, S.; Yano, J.; Stach, E. A.; Dincă, M. Signature of Metallic Behavior in the Metal—Organic Frameworks M ₃ (Hexaiminobenzene) ₂ (M = Ni, Cu). *J. Am. Chem. Soc.* **2017**, *139* (39), 13608–13611.
- (30) Xie, L. S.; Skorupskii, G.; Dincă, M. Electrically Conductive Metal-Organic Frameworks. *Chem. Rev.* **2020**, *120* (16), 8536–8580.
- (31) Huang, X.; Sheng, P.; Tu, Z.; Zhang, F.; Wang, J.; Geng, H.; Zou, Y.; Di, C.; Yi, Y.; Sun, Y.; Xu, W.; Zhu, D. A Two-Dimensional π -d Conjugated Coordination Polymer with Extremely High Electrical Conductivity and Ambipolar Transport Behaviour. *Nat. Commun.* **2015**, *6* (1), 7408.
- (32) Dong, R.; Han, P.; Arora, H.; Ballabio, M.; Karakus, M.; Zhang, Z.; Shekhar, C.; Adler, P.; Petkov, P. St.; Erbe, A.; Mannsfeld, S. C. B.; Felser, C.; Heine, T.; Bonn, M.; Feng, X.; Cánovas, E. High-Mobility Band-like Charge Transport in a Semiconducting Two-Dimensional Metal—Organic Framework. *Nat. Mater.* **2018**, *17* (11), 1027—1032.
- (33) Day, R. W.; Bediako, D. K.; Rezaee, M.; Parent, L. R.; Skorupskii, G.; Arguilla, M. Q.; Hendon, C. H.; Stassen, I.; Gianneschi, N. C.; Kim, P.; Dincă, M. Single Crystals of Electrically Conductive Two-Dimensional Metal—Organic Frameworks: Structural and Electrical Transport Properties. ACS Cent. Sci. 2019, 5 (12), 1959—1964.
- (34) Zhou, Q.; Wang, J.; Chwee, T. S.; Wu, G.; Wang, X.; Ye, Q.; Xu, J.; Yang, S.-W. Topological Insulators Based on 2D Shape-Persistent Organic Ligand Complexes. *Nanoscale* **2015**, 7 (2), 727–735.
- (35) Yamada, M. G.; Soejima, T.; Tsuji, N.; Hirai, D.; Dincă, M.; Aoki, H. First-Principles Design of a Half-Filled Flat Band of the Kagome Lattice in Two-Dimensional Metal-Organic Frameworks. *Phys. Rev. B* **2016**, *94* (8), 081102.
- (36) Wu, M.; Wang, Z.; Liu, J.; Li, W.; Fu, H.; Sun, L.; Liu, X.; Pan, M.; Weng, H.; Dinca, M.; Fu, L.; Li, J. Conetronics in 2D Metal-Organic Frameworks: Double/Half Dirac Cones and Quantum Anomalous Hall Effect. 2D Mater. 2017, 4 (1), 015015.
- (37) Zhang, X.; Wang, Z.; Zhao, M.; Liu, F. Tunable Topological States in Electron-Doped HTT-Pt. *Phys. Rev. B* **2016**, 93 (16), 165401.
- (38) Barreteau, C.; Ducastelle, F.; Mallah, T. A. A bird's eye view on the flat and conic band world of the honeycomb and Kagome lattices: towards an understanding of 2D metal-organic frameworks electronic structure. J. Phys.: Condens. Matter 2017, 29 (46), 465302.
- (39) Silveira, O. J.; Chacham, H. Electronic and Spin—Orbit Properties of the Kagome MOF Family M $_3$ (1,2,5,6,9, 10-Triphenylenehexathiol) $_2$ (M = Ni, Pt, Cu and Au). *J. Phys.: Condens. Matter* **2017**, 29 (9), 09LT01.
- (40) Deng, T.; Shi, W.; Wong, Z. M.; Wu, G.; Yang, X.; Zheng, J.-C.; Pan, H.; Yang, S.-W. Designing Intrinsic Topological Insulators in Two-Dimensional Metal—Organic Frameworks. *J. Phys. Chem. Lett.* **2021**, *12* (29), 6934–6940.

- (41) Gao, Z.; Gao, Y.; Hua, M.; Liu, J.; Huang, L.; Lin, N. Design and Synthesis of a Single-Layer Ferromagnetic Metal—Organic Framework with Topological Nontrivial Gaps. *J. Phys. Chem. C* **2020**, 124 (49), 27017–27023.
- (42) Sun, H.; Tan, S.; Feng, M.; Zhao, J.; Petek, H. Deconstruction of the Electronic Properties of a Topological Insulator with a Two-Dimensional Noble Metal—Organic Honeycomb—Kagome Band Structure. J. Phys. Chem. C 2018, 122 (32), 18659—18668.
- (43) Silveira, O. J.; Lima, É. N.; Chacham, H. Bilayers of Ni $_3$ C $_{12}$ S $_{12}$ and Pt $_3$ C $_{12}$ S $_{12}$: Graphene-like 2D Topological Insulators Tunable by Electric Fields. *J. Phys.: Condens. Matter* **2017**, 29 (46), 465502.
- (44) Crasto de Lima, F.; Ferreira, G. J.; Miwa, R. H. Layertronic Control of Topological States in Multilayer Metal-Organic Frameworks. *J. Chem. Phys.* **2019**, *150* (23), 234701.
- (45) Bachler, V.; Olbrich, G.; Neese, F.; Wieghardt, K. Theoretical Evidence for the Singlet Diradical Character of Square Planar Nickel Complexes Containing Two o -Semiquinonato Type Ligands. *Inorg. Chem.* **2002**, *41* (16), 4179–4193.
- (46) Herebian, D.; Wieghardt, K. E.; Neese, F. Analysis and Interpretation of Metal-Radical Coupling in a Series of Square Planar Nickel Complexes: Correlated Ab Initio and Density Functional Investigation of [Ni(L $^{\rm ISQ})_2$] (L $^{\rm ISQ}=3,5$ -Di- Tert -Butyl- o-Diiminobenzosemiquinonate(1-)). J. Am. Chem. Soc. 2003, 125 (36), 10997–11005.
- (47) Kaim, W. Manifestations of Noninnocent Ligand Behavior. *Inorg. Chem.* **2011**, *50* (20), 9752–9765.
- (48) Das, A.; Han, Z.; Brennessel, W. W.; Holland, P. L.; Eisenberg, R. Nickel Complexes for Robust Light-Driven and Electrocatalytic Hydrogen Production from Water. *ACS Catal.* **2015**, *5* (3), 1397–1406.
- (49) Vijaykumar, G.; Pariyar, A.; Ahmed, J.; Shaw, B. K.; Adhikari, D.; Mandal, S. K. Tuning the Redox Non-Innocence of a Phenalenyl Ligand toward Efficient Nickel-Assisted Catalytic Hydrosilylation. *Chem. Sci.* **2018**, *9* (10), 2817–2825.
- (50) Sikari, R.; Sinha, S.; Das, S.; Saha, A.; Chakraborty, G.; Mondal, R.; Paul, N. D. Achieving Nickel Catalyzed C-S Cross-Coupling under Mild Conditions Using Metal-Ligand Cooperativity. *J. Org. Chem.* **2019**, *84* (7), 4072–4085.
- (51) Miner, E. M.; Gul, S.; Ricke, N. D.; Pastor, E.; Yano, J.; Yachandra, V. K.; Van Voorhis, T.; Dincă, M. Mechanistic Evidence for Ligand-Centered Electrocatalytic Oxygen Reduction with the Conductive MOF Ni ₃ (Hexaiminotriphenylene) ₂. ACS Catal. **2017**, 7 (11), 7726–7731.
- (52) Feng, D.; Lei, T.; Lukatskaya, M. R.; Park, J.; Huang, Z.; Lee, M.; Shaw, L.; Chen, S.; Yakovenko, A. A.; Kulkarni, A.; Xiao, J.; Fredrickson, K.; Tok, J. B.; Zou, X.; Cui, Y.; Bao, Z. Robust and Conductive Two-Dimensional Metal—organic Frameworks with Exceptionally High Volumetric and Areal Capacitance. *Nat. Energy* 2018, 3 (1), 30–36.
- (53) Stiefel, E. I.; Waters, J. H.; Billig, E.; Gray, H. B. The Myth of Nickel(III) and Nickel(IV) in Planar Complexes ¹. *J. Am. Chem. Soc.* **1965**, *87* (13), 3016–3017.
- (54) Malrieu, J. P.; Caballol, R.; Calzado, C. J.; de Graaf, C.; Guihéry, N. Magnetic Interactions in Molecules and Highly Correlated Materials: Physical Content, Analytical Derivation, and Rigorous Extraction of Magnetic Hamiltonians. *Chem. Rev.* **2014**, *114* (1), 429–492.
- (55) Stuyver, T.; Chen, B.; Zeng, T.; Geerlings, P.; De Proft, F.; Hoffmann, R. Do Diradicals Behave Like Radicals? *Chem. Rev.* **2019**, 119 (21), 11291–11351.
- (56) Gräfenstein, J.; Hjerpe, A. M.; Kraka, E.; Cremer, D. An Accurate Description of the Bergman Reaction Using Restricted and Unrestricted DFT: Stability Test, Spin Density, and On-Top Pair Density. *J. Phys. Chem. A* **2000**, *104* (8), 1748–1761.
- (57) Caballol, R.; Castell, O.; Illas, F.; de P R Moreira, I.; Malrieu, J. P. Remarks on the Proper Use of the Broken Symmetry Approach to Magnetic Coupling. *J. Phys. Chem. A* **1997**, *101* (42), 7860–7866.

- (58) Park, J.; Lee, M.; Feng, D.; Huang, Z.; Hinckley, A. C.; Yakovenko, A.; Zou, X.; Cui, Y.; Bao, Z. Stabilization of Hexaaminobenzene in a 2D Conductive Metal—Organic Framework for High Power Sodium Storage. *J. Am. Chem. Soc.* **2018**, *140* (32), 10315—10323.
- (59) Eremenko, I. L.; Nefedov, S. E.; Sidorov, A. A.; Ponina, M. O.; Danilov, P. V.; Stromnova, T. A.; Stolarov, I. P.; Katser, S. B.; Orlova, S. T.; Vargaftik, M. N.; Moiseev, I. I.; Ustynyuk, Yu. A. Imido/Nitrene Ligands in the Complexes of Platinum Metals. *J. Organomet. Chem.* 1998, 551 (1–2), 171–194.
- (60) Jovanovic, M.; Schoop, L. M. Simple Chemical Rules for Predicting Band Structures of Kagome Materials. J. Am. Chem. Soc. 2022, 144 (24), 10978–10991.
- (61) Johnston, R. L.; Hoffmann, R. The Kagomé Net: Band Theoretical and Topological Aspects. *Polyhedron* **1990**, 9 (15–16), 1901–1911.
- (62) Liu, Z.; Wang, Z.-F.; Mei, J.-W.; Wu, Y.-S.; Liu, F. Flat Chern Band in a Two-Dimensional Organometallic Framework. *Phys. Rev. Lett.* **2013**, *110* (10), 106804.
- (63) Su, N.; Jiang, W.; Wang, Z.; Liu, F. Prediction of Large Gap Flat Chern Band in a Two-Dimensional Metal-Organic Framework. *Appl. Phys. Lett.* **2018**, *112* (3), 033301.
- (64) Regnault, N.; Xu, Y.; Li, M.-R.; Ma, D.-S.; Jovanovic, M.; Yazdani, A.; Parkin, S. S. P.; Felser, C.; Schoop, L. M.; Ong, N. P.; Cava, R. J.; Elcoro, L.; Song, Z.-D.; Bernevig, B. A. Catalogue of Flat-Band Stoichiometric Materials. *Nature* **2022**, *603* (7903), 824–828.
- (65) Berry, T.; Morey, J. R.; Arpino, K. E.; Dou, J.-H.; Felser, C.; Dincă, M.; McQueen, T. M. Structural, Thermodynamic, and Transport Properties of the Small-Gap Two-Dimensional Metal—Organic Kagomé Materials Cu ₃ (Hexaiminobenzene) ₂ and Ni ₃ (Hexaiminobenzene) ₂. *Inorg. Chem.* **2022**, *61* (17), 6480–6487.
- (66) Posternak, M.; Baldereschi, A.; Freeman, A. J.; Wimmer, E.; Weinert, M. Prediction of Electronic Interlayer States in Graphite and Reinterpretation of Alkali Bands in Graphite Intercalation Compounds. *Phys. Rev. Lett.* **1983**, *50* (10), 761–764.
- (67) Catellani, A.; Posternak, M.; Baldereschi, A.; Jansen, H. J. F.; Freeman, A. J. Electronic Interlayer States in Hexagonal Boron Nitride. *Phys. Rev. B* **1985**, 32 (10), 6997–6999.
- (68) Inoshita, T.; Saito, S.; Hosono, H. Floating Interlayer and Surface Electrons in 2D Materials: Graphite, Electrides, and Electrenes. *Small Sci.* **2021**, *1* (9), 2100020.
- (69) Csányi, G.; Littlewood, P. B.; Nevidomskyy, A. H.; Pickard, C. J.; Simons, B. D. The Role of the Interlayer State in the Electronic Structure of Superconducting Graphite Intercalated Compounds. *Nature Phys.* **2005**, *1* (1), 42–45.
- (70) Zurek, E.; Jepsen, O.; Andersen, O. K. Muffin-Tin Orbital Wannier-Like Functions for Insulators and Metals. *ChemPhysChem* **2005**, *6* (9), 1934–1942.
- (71) Rousseau, B.; Ashcroft, N. W. Interstitial Electronic Localization. *Phys. Rev. Lett.* **2008**, *101* (4), 046407.
- (72) Miao, M.-S.; Hoffmann, R. High Pressure Electrides: A Predictive Chemical and Physical Theory. *Acc. Chem. Res.* **2014**, 47 (4), 1311–1317.
- (73) Dai, D.; Xiang, H.; Whangbo, M.-H. Effects of Spin-Orbit Coupling on Magnetic Properties of Discrete and Extended Magnetic Systems. *J. Comput. Chem.* **2008**, 29 (13), 2187–2209.
- (74) Fu, L.; Kane, C. L. Topological Insulators with Inversion Symmetry. *Phys. Rev. B* **2007**, *76* (4), 045302.
- (75) Dou, J.-H.; Arguilla, M. Q.; Luo, Y.; Li, J.; Zhang, W.; Sun, L.; Mancuso, J. L.; Yang, L.; Chen, T.; Parent, L. R.; Skorupskii, G.; Libretto, N. J.; Sun, C.; Yang, M. C.; Dip, P. V.; Brignole, E. J.; Miller, J. T.; Kong, J.; Hendon, C. H.; Sun, J.; Dincă, M. Atomically Precise Single-Crystal Structures of Electrically Conducting 2D Metal—Organic Frameworks. *Nat. Mater.* 2021, 20 (2), 222–228.
- (76) Beaudoin, D.; Maris, T.; Wuest, J. D. Constructing Monocrystalline Covalent Organic Networks by Polymerization. *Nature Chem.* **2013**, *5* (10), 830–834.
- (77) Tang, W.; Zhao, Y.; Xu, M.; Xu, J.; Meng, S.; Yin, Y.; Zhang, Q.; Gu, L.; Liu, D.; Gu, Z. Controlling the Stacking Modes of Metal—

- Organic Framework Nanosheets through Host-Guest Noncovalent Interactions. *Angew. Chem. Int. Ed* **2021**, *60* (13), 6920–6925.
- (78) Tang, W.-Q.; Yi, X.; Guan, H.; Wang, X.-W.; Gu, Y.-W.; Zhao, Y.-J.; Fu, J.; Li, W.; Cheng, Y.; Meng, S.-S.; Xu, M.; Zhang, Q.-H.; Gu, L.; Kong, X.; Liu, D.-H.; Wang, W.; Gu, Z.-Y. Bipolar Molecular Torque Wrench Modulates the Stacking of Two-Dimensional Metal—Organic Framework Nanosheets. *J. Am. Chem. Soc.* **2023**, *145* (49), 26580–26591.
- (79) Cheng, Y.; Tang, W.-Q.; Geng, L.-T.; Xu, M.; Zhu, J.-P.; Meng, S.-S.; Gu, Z.-Y. Polar Alcohol Guest Molecules Regulate the Stacking Modes of 2-D MOF Nanosheets. *Chem. Sci.* **2024**, *15* (11), 4106–4113.
- (80) Lu, Y.; Hu, Z.; Petkov, P.; Fu, S.; Qi, H.; Huang, C.; Liu, Y.; Huang, X.; Wang, M.; Zhang, P.; Kaiser, U.; Bonn, M.; Wang, H. I.; Samori, P.; Coronado, E.; Dong, R.; Feng, X. Tunable Charge Transport and Spin Dynamics in Two-Dimensional Conjugated Metal—Organic Frameworks. *J. Am. Chem. Soc.* **2024**, *146* (4), 2574—2582.
- (81) Ray, K.; Petrenko, T.; Wieghardt, K.; Neese, F. Joint Spectroscopic and Theoretical Investigations of Transition Metal Complexes Involving Non-Innocent Ligands. *Dalton Trans.* **2007**, No. 16, 1552.
- (82) Fischer, D. A.; Wentzcovitch, R. M.; Carr, R. G.; Continenza, A.; Freeman, A. J. Graphitic Interlayer States: A Carbon K near-Edge x-Ray-Absorption Fine-Structure Study. *Phys. Rev. B* **1991**, *44* (3), 1427–1429.
- (83) Selloni, A.; Chen, C. D.; Tosatti, E. Scanning Tunneling Spectroscopy of Graphite and Intercalates. *Phys. Scr.* **1988**, *38* (2), 297–300.
- (84) Giannozzi, P.; Baroni, S.; Bonini, N.; Calandra, M.; Car, R.; Cavazzoni, C.; Ceresoli, D.; Chiarotti, G. L.; Cococcioni, M.; Dabo, I.; Dal Corso, A.; de Gironcoli, S.; Fabris, S.; Fratesi, G.; Gebauer, R.; Gerstmann, U.; Gougoussis, C.; Kokalj, A.; Lazzeri, M.; Martin-Samos, L.; Marzari, N.; Mauri, F.; Mazzarello, R.; Paolini, S.; Pasquarello, A.; Paulatto, L.; Sbraccia, C.; Scandolo, S.; Sclauzero, G.; Seitsonen, A. P.; Smogunov, A.; Umari, P.; Wentzcovitch, R. M. QUANTUM ESPRESSO: A Modular and Open-Source Software Project for Quantum Simulations of Materials. *J. Phys.: Condens. Matter* 2009, 21 (39), 395502.
- (85) Giannozzi, P.; Andreussi, O.; Brumme, T.; Bunau, O.; Buongiorno Nardelli, M.; Calandra, M.; Car, R.; Cavazzoni, C.; Ceresoli, D.; Cococcioni, M.; Colonna, N.; Carnimeo, I.; Dal Corso, A.; de Gironcoli, S.; Delugas, P.; DiStasio, R. A.; Ferretti, A.; Floris, A.; Fratesi, G.; Fugallo, G.; Gebauer, R.; Gerstmann, U.; Giustino, F.; Gorni, T.; Jia, J.; Kawamura, M.; Ko, H.-Y.; Kokalj, A.; Küçükbenli, E.; Lazzeri, M.; Marsili, M.; Marzari, N.; Mauri, F.; Nguyen, N. L.; Nguyen, H.-V.; Otero-de-la-Roza, A.; Paulatto, L.; Poncé, S.; Rocca, D.; Sabatini, R.; Santra, B.; Schlipf, M.; Seitsonen, A. P.; Smogunov, A.; Timrov, I.; Thonhauser, T.; Umari, P.; Vast, N.; Wu, X.; Baroni, S. Advanced Capabilities for Materials Modelling with Quantum ESPRESSO. J. Phys.: Condens. Matter 2017, 29 (46), 465901.
- (86) Rappe, A. M.; Rabe, K. M.; Kaxiras, E.; Joannopoulos, J. D. Optimized Pseudopotentials. *Phys. Rev. B* **1990**, *41* (2), 1227–1230. (87) Grimme, S.; Ehrlich, S.; Goerigk, L. Effect of the Damping Function in Dispersion Corrected Density Functional Theory. *J. Comput. Chem.* **2011**, 32 (7), 1456–1465.
- (88) Periodic DFT: BAND and Quantum Espresso. https://www.scm.com/amsterdam-modeling-suite/periodic-dft-band-quantum-espresso/ (accessed June 4, 2023).
- (89) Wiesenekker, G.; Baerends, E. J. Quadratic Integration over the Three-Dimensional Brillouin Zone. *J. Phys.: Condens. Matter* **1991**, 3 (35), 6721–6742.
- (90) Philipsen, P. H. T.; van Lenthe, E.; Snijders, J. G.; Baerends, E. J. Relativistic Calculations on the Adsorption of CO on the (111) Surfaces of Ni, Pd, and Pt within the Zeroth-Order Regular Approximation. *Phys. Rev. B* **1997**, *56* (20), 13556–13562.